Ru/MgO catalyst with dual Ru structure sites for efficient CO production from CO_2 hydrogenation

Shaohua Xie,[a,†] Kailong Ye,[a,†] Jingshan S. Du,[b,†] Xing Zhang,[a] Daekun Kim,[a] Jeremia Loukusa,[a] Lu Ma,[d] Steven N. Ehrlich,[d] Nebojsa S. Marinkovic,[e] James J. De Yoreo,[b,c] Fudong Liu[a,*]

[a] Department of Chemical and Environmental Engineering, University of California, Riverside, California 92521, United States

[b] Department of Civil, Environmental, and Construction Engineering, Catalysis Cluster for Renewable Energy and Chemical Transformations (REACT), NanoScience Technology Center (NSTC), University of Central Florida, Orlando, FL 32816, United States

[c] Physical Sciences Division, Pacific Northwest National Laboratory, Richland, WA 99352, United States

[d] Department of Materials Science and Engineering, University of Washington, Seattle, WA 98195, United States

[e] National Synchrotron Light Source II (NSLS-II), Brookhaven National Laboratory, Upton, NY 11973, United States

[f] Department of Chemical Engineering, Columbia University, New York, NY 10027, United States

[†] These authors contributed equally to this work.

*Corresponding author. Email address: fudong.liu@ucf.edu (F.L.)

Abstract

The development and comprehension of supported metal catalysts for CO_2 hydrogenation is of paramount importance in mitigating the net CO_2 emissions. Supported Ru catalysts have been widely recognized in facilitating CO_2 methanation, on which recent findings suggest that the CO_2 hydrogenation process can be manipulated to favor the reverse water-gas shift (RWGS) pathway by precisely adjusting the size of Ru particles. However, the size-dependent impact of Ru remains a topic of lively debate. In this work, Ru/MgO catalysts with Ru in the form of single atoms (Ru_1) and atomic single-layer (Ru_{ASL}) structures were prepared for CO_2 hydrogenation. The 1.0Ru/MgO catalyst (with 1 wt.% of Ru), featuring a mixture of Ru_1 and Ru_{ASL} with a size of 0.6-1.0 nm, showed the highest CO yield (38% at 500 °C) with balanced CO_2 conversion and CO selectivity. Transient CO_2 hydrogenation and temperature-programmed surface reaction (TPSR) studies suggested that the adsorbed CO_2 species participated in CO_2 hydrogenation. On Ru_1 sites, CO_2 hydrogenation followed the RWGS pathway, resulting in the production of CO. In contrast, on Ru_{ASL} sites, the enhanced H_2 dissociation ability, along with the presence of adsorbed bidentate and monodentate carbonate species at the Ru-MgO interfaces, facilitated the formation of CH_4 through the CO_2 methanation pathway. This study highlights the critical roles of Ru structure and local environment in defining the CO_2 hydrogenation pathways and provides new design principles for highly active Ru-based catalysts.

Keywords: CO_2 hydrogenation; Ru/MgO; Single-atom catalyst; Atomic single-layer structure; Reaction mechanism.

1. Introduction

Catalytic CO_2 hydrogenation holds significant promise to convert CO_2, a major greenhouse emission, to high-value products, including fuels and essential building blocks in the chemical industry.[1-3] At atmospheric pressure, this process primarily results in the formation of CH_4 through CO_2 methanation,[4, 5] and CO through the reverse water-gas shift (RWGS) reaction[6, 7]. CO_2 methanation serves the purpose of generating synthetic natural gas,[8, 9] while RWGS produces CO,[6, 10] a versatile raw material for producing value-added products through processes such as the Fischer-Tropsch synthesis.[1, 6, 11, 12] For CO_2 hydrogenation, the catalyst ability to activate H_2 and/or facilitate CO desorption plays a pivotal role in determining the dominant reaction pathway.[13, 14] It is generally agreed that a more favorable CO desorption capability and a weaker H_2 activation ability will better facilitate the RWGS pathway. In supported metal catalysts, large metal clusters typically prove advantageous for H_2 activation, thus facilitating deep CO_2 reduction and suppressing CO production.[15] Conversely, metal single atoms or small clusters exhibit lower activity in H_2 activation, resulting in a higher CO selectivity via the RWGS pathway. Accordingly, whether it is the relatively low CO selectivity on large metal clusters or the poor CO_2 hydrogenation activity on metal single atoms or small clusters, both scenarios lead to a diminished CO yield in CO_2 hydrogenation. Therefore, to enhance the efficiency of CO production, precise control of metal structure and size becomes imperative, thus striking the right balance between CO_2 hydrogenation activity and CO selectivity.

Supported ruthenium (Ru) catalysts are typically considered one type of the most active and stable catalysts for CO_2 methanation due to their capability to dissociate H_2 and bind CO.[3, 16-23] However, recent findings suggest that the CO_2 methanation pathway on Ru catalysts could be altered towards the RWGS pathway.[24-26] For example, by constructing strong metal-support interaction in Ru-MoO_3 catalyst using CO_2 hydrogenation reaction gas at 250 °C, it was possible to create MoO_{3-x} overlayers on Ru particles within the Ru@MoO_{3-x} catalyst.[25] Consequently, the initially observed 100% CH_4 selectivity on Ru-MoO_3 could be transformed to an impressive selectivity of over 99% CO on Ru@MoO_{3-x}, while maintaining excellent activity and long-term catalytic stability. Additionally, the H-SiO_2@Ru@SiO_2 catalyst by encapsulating 1 nm Ru clusters within hollow silica shells has shown remarkable performance in CO_2 hydrogenation.[26] This catalyst not only demonstrated outstanding CO_2 reduction activity but also exhibited nearly 100% selectivity for CO. In addition, recent studies have also suggested that the size of Ru clusters played

a crucial role in determining the CO_2 hydrogenation pathway. When supported on Al_2O_3, it was reported that Ru single atoms and small clusters exhibited high selectivity towards the RWGS pathway, whereas larger Ru particles tend to favor CH_4 formation.[27] In the case of Ru nanoparticles supported on CeO_2, an oxidative pretreatment could induce the redispersion of Ru nanoparticles into atomically dispersed sites, and result in a complete switch in the performance from a well-known selective methanation catalyst to an active and selective RWGS catalyst.[24] However, it is important to note that the size-dependent effect is still a subject of debate in the literature, as numerous reports suggest that the supported Ru-based materials are effective CO_2 methanation catalysts, regardless of whether the Ru species exist as single atoms or clusters.[5, 28-31] For instance, either it was Ru-doped CeO_2[31] or Ru single atoms and clusters (1-3 nm) supported on CeO_2,[28] they all functioned as active methanation catalysts demonstrating >99% CH_4 selectivity.

To elucidate how Ru structure and local environment affect the CO_2 hydrogenation pathway and to unveil the active Ru sites responsible for achieving high CO yield via the RWGS reaction, herein, we proposed a catalytic system comprising MgO as a support and Ru species with varying sizes and structures as the active sites. MgO was chosen as the support material because, as a Lewis base, it is effective in capturing CO_2.[32, 33] Moreover, MgO can effectively mitigate catalyst deactivation arising from active site sintering and carbon deposition (*i.e.*, coking).[34, 35] Our study revealed that the Ru species ranging from single atoms to large clusters could be synthesized by increasing the Ru density on the MgO support. As the size of the Ru clusters in Ru/MgO increased, we observed a corresponding increase in the CO_2 hydrogenation activity. Among all the catalysts tested, 1.0Ru/MgO (with 1 wt.% of Ru) showing both Ru single atoms (Ru_1) and Ru atomic single-layer (Ru_{ASL}, with cluster size of *ca.* 0.6-1.0 nm) achieved the highest CO yield. By performing temperature-programmed surface reaction and transient CO_2 hydrogenation experiments, CO_2 hydrogenation pathways on different Ru structures were investigated. This work underscores the pivotal role of Ru structure in dictating the CO_2 hydrogenation pathway on Ru/MgO catalysts, which is important for their potential industrial applications.

2. Materials and methods

2.1. Materials

Magnesium hydroxide ($Mg(OH)_2$) and ruthenium (III) nitrosyl nitrate (31.3 wt.% Ru) were

100 purchased from Alfa Aesar. H_2 (99.99 %), CO_2 (99.99 %), O_2 (99.99 %), 10% H_2/Ar, and Ar
101 (99.999 %) gas cylinders were purchased from Airgas. No further treatment was conducted on all
102 chemicals and cylinders used in this work.

103 **2.2. Catalyst preparation**

104 The *x*Ru/MgO catalysts with *x* wt.% Ru (*x* = 0.5, 0.625, 0.75, 1.0 or 2.0) were prepared by a
105 conventional incipient wetness impregnation (IWI) method, using $Mg(OH)_2$ as support and
106 ruthenium(III) nitrosyl nitrate as precursor. Typically, a solution of ruthenium (III) nitrosyl nitrate
107 with determined concentration was added dropwise onto $Mg(OH)_2$ support under stirring.
108 Following a dehydration at 120 °C for 1 h, the obtained powders were calcined at 550 °C for 2 h
109 with a temperature ramp of 5 °C/min. For comparison, the reference catalyst 1.0Ru/MgO-ref was
110 prepared using the same method for 1.0Ru/MgO, except that MgO (obtained by the calcination of
111 $Mg(OH)_2$ at 800 °C for 2 h) was used as support.

112 **2.3. Characterization**

113 X-ray powder diffraction (XRD) patterns were obtained using a PANalytical Empyrean
114 diffractometer, utilizing Cu Kα X-rays with a wavelength of 0.15406 nm. The XRD patterns were
115 collected within the range of 10 to 80 °, employing a scanning speed of 6 °/min and a scanning
116 step of 0.067 °.

117 The porosity property of the samples was determined via N_2 physisorption at 77 K using a liquid
118 nitrogen bath on a Quantachrome Physisorption-Chemisorption Instrument (Autosorb-iQ), with
119 the samples degassed at 300 °C for 1 h under vacuum before measurement. Brunauer-Emmett-
120 Teller (BET) surface areas were calculated using adsorption points in the relative pressures
121 between 0.05 and 0.3. The non-local density functional theory (DFT) method was used to
122 determine the pore size distributions of the samples.

123 Transmission electron microscopy (TEM) imaging and electron diffraction were performed for
124 the *x*Ru/MgO samples (*x* = 0.5, 0.625, 0.75, and 1.0) using an FEI Titan (Schottky field-emission
125 gun (FEG), 300 kV) with a CEOS double-hexapole aberration corrector for the image-forming
126 lenses, and for the 2.0Ru/MgO sample using an FEI Tecnai F30 (Schottky FEG, 300 kV). Scanning
127 transmission electron microscopy (STEM) imaging was performed on a JEOL JEM-ARM300CF
128 GRAND ARM (cold FEG, 300 kV) with a JEOL dodecapole aberration corrector for the probe-

129 forming lenses. The high-angle annular dark-field imaging (HAADF) collection angle was 68−280
130 mrad. High-magnification HAADF images were denoised using a non-linear filter described in an
131 earlier report.[36] Energy dispersive X-ray spectroscopy (EDS) data was captured on the JEM-
132 ARM300CF with dual JEOL Centurio silicon drift detectors (SDDs) and processed with Thermo
133 Fisher Pathfinder for elemental mapping based on net signal counts and standardless quantification.

134 X-ray absorption near edge structure (XANES) and extended X-ray absorption fine structure
135 (EXAFS) of Ru K-edge for the selected samples were measured in fluorescent mode at beamline
136 7-BM QAS of the National Synchrotron Light Source II (NSLS-II), Brookhaven National
137 Laboratory. *Ex situ* measurements were performed at room temperature (RT). For *in situ*
138 measurements, following the loading of 100 mg sample into the Nashner-Adler reaction cell, the
139 experiments were conducted as follows: Step 1, the N_2 flow at a rate of 20 mL/min was introduced
140 at 30 °C and maintained for 10 min before collecting Spectrum 1; Step 2, the flow was
141 subsequently switched to 10% CO_2 + 30% H_2 (CO_2 + H_2) mixture with N_2 balance (20 mL/min),
142 and the sample was maintained at 30 °C for 10 min before collecting Spectrum 2; Step 3, in the
143 same CO_2 + H_2 flow, the sample was heated from 30 to 500 °C and maintained at 500 °C for 30
144 min;, and then Spectrum 3 was collected; Step 4, the flow was then adjusted to 10% CO_2 (using
145 N_2 as balance) at a rate of 20 mL/min and maintained at 500 °C for 30 min before collecting
146 Spectrum 4; Step 5, subsequently, the flow was switched back to the CO_2 + H_2 mixture (20 mL/min)
147 and maintained at 500 °C for 30 min before collecting Spectrum 5; Step 6, the sample was cooled
148 down to 30 °C in the same CO_2 + H_2 flow, and Spectrum 6 was collected after holding for 10 min.
149 Data were analyzed using Athena and Artemis from the Demeter software package. Ru foil was
150 measured during data collection for energy calibration and drift correction of the monochromator.
151 The processed EXAFS, $\chi(k)$, was weighted by k^2 to amplify the high-k oscillations. For Fourier-
152 transformed (FT) spectra, the k range between 3 and 12 $Å^{-1}$ was used, and the fitting in the R range
153 for Ru coordination shells was between 1.0 and 3.0 Å for Ru/MgO samples, and between 1.5 and
154 3.0 Å for Ru foil in Artemis software.

155 H_2 temperature-programmed reduction (H_2-TPR) experiment was carried out on a
156 Quantachrome Physisorption-Chemisorption Instrument (Autosorb-iQ). Prior to testing, all
157 samples were pretreated in a flow of 5 % O_2/He (40 mL/min) at 500 °C for 1 h to remove potential
158 surface adsorbents. After cooling down to 40 °C, the pretreated sample was exposed to a flow of
159 10 % H_2/Ar (30 mL/min), and heated linearly from 40 to 850 °C at a ramping rate of 10 °C/min.

160 The alteration in H_2 concentration was monitored on-line using a thermal conductivity detector
161 (TCD). The H_2 consumption of each sample was calculated using CuO as standard.

162 CO_2 temperature-programmed desorption (CO_2-TPD) and H_2 temperature-programmed surface
163 reaction (H_2-TPSR) experiments were performed in a fixed-bed quartz tube reactor. Prior to testing,
164 50 mg of sample was loaded and pretreated in 20% O_2/Ar flow (40 mL·min^{-1}) at 350 °C for 30
165 min. Afterwards, the sample was exposed to 10% CO_2/Ar flow (40 mL·min^{-1}) to achieve saturated
166 CO_2 adsorption at 40 °C. The flow was then switched to pure Ar (40 mL/min) for 30 min to remove
167 weakly adsorbed CO_2. For the CO_2-TPD experiment, the sample was heated linearly from 40 to
168 700 °C in Ar flow at a ramping rate of 10 °C/min. In the case of H_2-TPSR, instead of heating in
169 Ar flow as that in CO_2-TPD, the sample was exposed to 10% H_2/Ar flow (40 mL·min^{-1}) and heated
170 from 40 to 700 °C with a ramping rate of 10 °C/min. The concentrations of CO_2, H_2, CO, and CH_4
171 were continuously monitored using a mass spectrometer (MS, Hiden Analytical HPR20 R&D)
172 with *m*/*z* values of 44, 2, 28, and 15, respectively.

173 *In situ* diffused reflectance infrared Fourier transform spectroscopy (DRIFTS) experiments were
174 carried out on a Thermo Nicolet iS50 FTIR spectrometer with a liquid nitrogen-cooling mercury-
175 cadmium-telluride (MCT) detector. The infrared (IR) spectra were recorded by accumulating 100
176 scans at a spectral resolution of 4 cm^{-1}. Before *in situ* DRIFTS experiment, catalyst was loaded
177 into a high-temperature IR cell (PIKE DiffusIR cell with ZnSe windows), followed by a treatment
178 in 10 % O_2/Ar flow (30 mL/min) at 400 °C for 1 h. Subsequently, the catalyst was cooled to 25 °C
179 followed by Ar purge (50 mL/min) for 30 min before collecting background spectrum. For CO_2
180 adsorption, typically, 2.5% CO_2/Ar was introduced into the cell for 1 h to achieve saturated CO_2
181 adsorption on the catalyst. Then, the flow of CO_2 was discontinued, and the catalyst was exposed
182 to Ar flow for 30 min to remove weakly adsorbed CO_2. The IR spectra were collected continuously
183 during the whole procedures.

184 **2.4. Evaluation of catalytic performance**

185 Catalytic performance of Ru/MgO catalysts for the RWGS reaction was evaluated on a continuous
186 flow fixed-bed quartz tubular microreactor (internal diameter = 4.0 mm). Typically, 25 mg of
187 catalyst (40-60 mesh) diluted with 0.25 g SiC (40-60 mesh) was loaded into the reactor to achieve
188 a weight hourly space velocity (WHSV) of 200 L·g_{cat}^{-1}·h^{-1}. For apparent activation energy
189 measurement, 12.5 mg of catalyst was used, achieving the WHSV of 400 L·g_{cat}^{-1}·h^{-1}. In addition,

to exclude the Ru loading effect, varied WHSV was also used for Ru/MgO catalyst with different Ru loadings, obtaining the WHSV of 40,000 $L \cdot g_{Ru}^{-1} \cdot h^{-1}$ normalized by Ru content. The feeding gas was composed of 30 % H_2 and 10 % CO_2 using Ar as balance. The concentrations of CO_2, CO, and CH_4 were detected online using a gas chromatography-mass spectrometry (GC-MS, Shimadzu, QP2010 SE). The CO_2 conversion, CO selectivity, and CO yield during the RWGS reaction were determined according to the following equations:

$$CO_2 \text{ conversion } (\%) = ([CO_2]_{in} - [CO_2]_{out}) / [CO_2]_{in} \times 100\% \quad (1)$$

$$CO \text{ selectivity } (\%) = [CO]_{out} / ([CO_2]_{in} - [CO_2]_{out}) \times 100\% \quad (2)$$

$$CO \text{ yield } (\%) = [CO]_{out} / [CO_2]_{in} \times 100\% \quad (3)$$

3. Results and discussion

3.1. Catalytic CO_2 hydrogenation performance

Fig. 1 shows the catalytic performance of CO_2 hydrogenation on the as-prepared Ru/MgO catalysts with different Ru loadings. Under the testing conditions using a weight hourly space velocity (WHSV) of 200 $L \cdot g_{cat}^{-1} \cdot h^{-1}$ based on the mass of catalyst, as depicted in **Fig. 1a**, the CO_2 conversion on Ru/MgO catalysts exhibited a significant upward trend as the Ru loading increased from 0.5 to 2.0 wt.%. Conversely, as shown in **Fig. S1a**, the CO selectivity gradually declined as a function of elevated Ru loading, decreasing from 100% to 48% at 500 °C due to the formation of CH_4. To better demonstrate the CO_2 hydrogenation performance, we calculated the CO yields on different catalysts, and the results are presented in **Fig. 1b**. As the Ru loading increased from 0.5 to 1.0 wt.%, the CO yield at 500 °C exhibited a significant increase, rising from 4% on 0.5Ru/MgO to 38% on 1.0Ru/MgO. However, when the Ru loading was further increased to 2 wt.%, the CO yield decreased to 23%. The 1.0Ru/MgO catalyst performed the best, demonstrating the highest CO yield among all the catalysts.

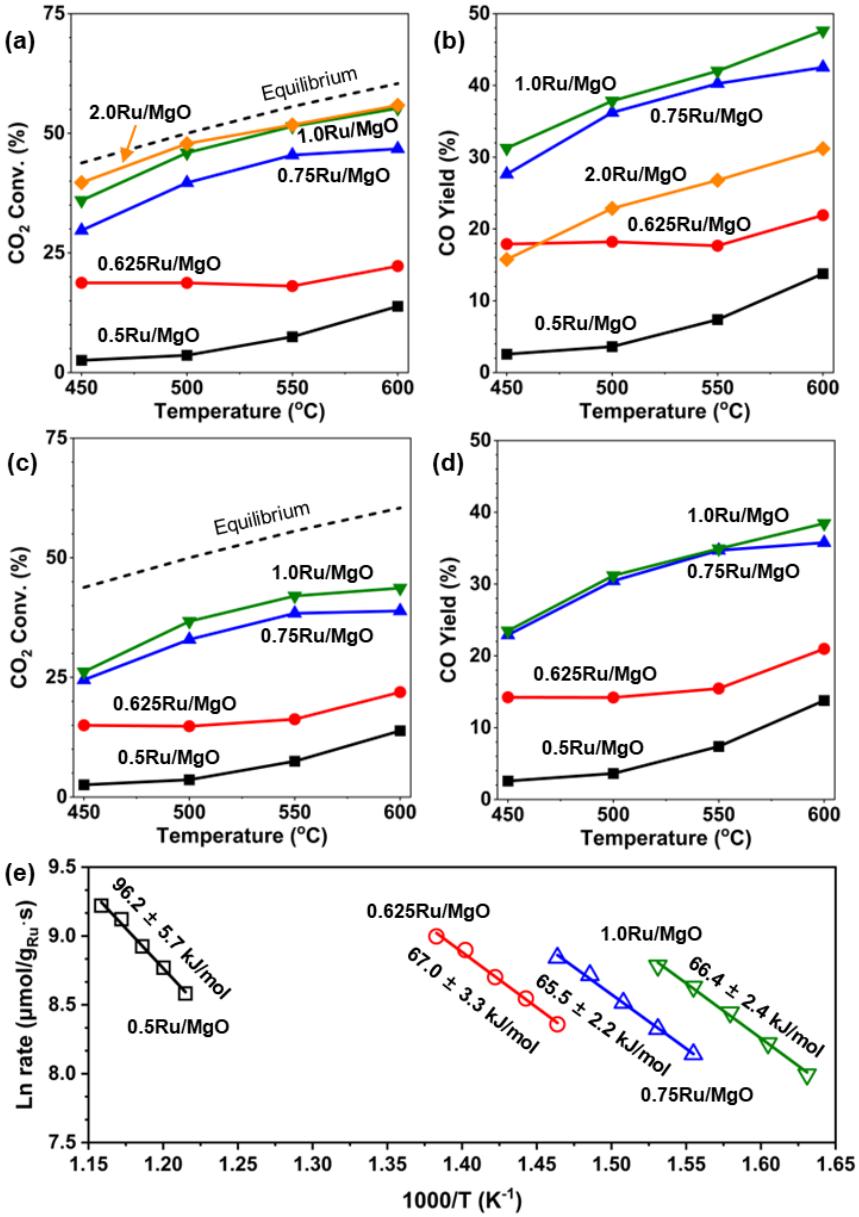

Fig. 1. (a) CO_2 conversion and (b) CO yield on 0.5Ru/MgO, 0.625Ru/MgO, 0.75Ru/MgO, 1.0Ru/MgO, and 2.0Ru/MgO catalysts under RWGS testing condition with a weight hourly space velocity (WHSV) of 200 $L \cdot g_{cat}^{-1} \cdot h^{-1}$. (c) CO_2 conversion and (d) CO yield on 0.5Ru/MgO, 0.625Ru/MgO, 0.75Ru/MgO, and 1.0Ru/MgO catalysts under RWGS testing condition with a WHSV of 40,000 $L \cdot g_{Ru}^{-1} \cdot h^{-1}$ normalized by Ru content. (e) Arrhenius plots of RWGS rates on 0.5Ru/MgO, 0.625Ru/MgO, 0.75Ru/MgO, and 1.0Ru/MgO catalysts; Reaction conditions for determination of apparent activation energy: 10% CO_2, 30% H_2; WHSV: 400 $L \cdot g_{cat}^{-1} \cdot h^{-1}$, with CO_2 conversion controlled below 13%.

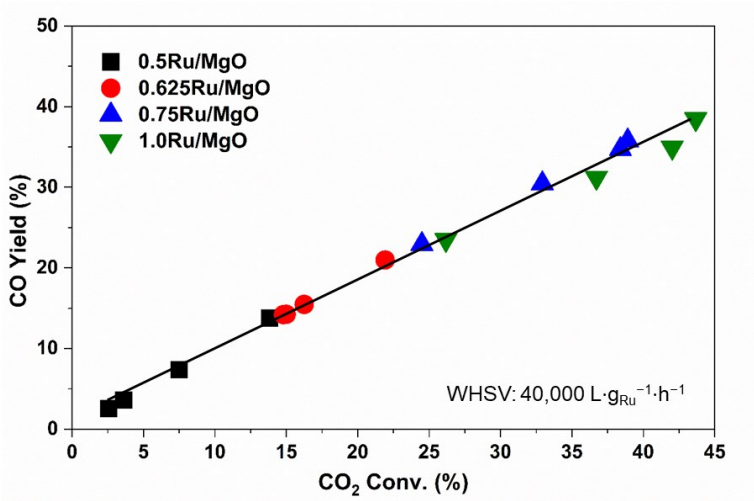

Fig. 2. CO yield as a function of CO_2 conversion over 0.5Ru/MgO, 0.625Ru/MgO, 0.75Ru/MgO, and 1.0Ru/MgO catalysts under the RWGS testing condition with a WHSV of 40,000 $L \cdot g_{Ru}^{-1} \cdot h^{-1}$ normalized by Ru content.

To confirm the active Ru sites for CO_2 hydrogenation, we conducted further assessment of the Ru/MgO catalysts, utilizing a WHSV of 40,000 $L \cdot g_{Ru}^{-1} \cdot h^{-1}$ normalized by the mass of Ru in the catalysts. By doing so, we aimed to exclude the effect of Ru loading on the CO_2 hydrogenation performance. As depicted in **Figs. 1c**, **1d** and **S1b**, similar CO_2 conversion trends emerged when comparing to the results obtained under the testing conditions using WHSV of 200 $L \cdot g_{cat}^{-1} \cdot h^{-1}$. Notably, as the Ru loading increased from 0.5 to 1.0 wt.%, the Ru sites within the Ru/MgO catalysts exhibited monotonically improved activity in CO_2 hydrogenation. This increase was evident through both the improved CO_2 conversions (**Fig. 1c**) and the higher CO yields (**Fig. 1d**) with elevated Ru loading or density, even though there was some decrease in the CO selectivity (**Fig. S1b**). To gain a deeper insight into the Ru sites, the relationship between CO yield and CO_2 conversion in the CO_2 hydrogenation reaction was established. As depicted in **Fig. 2**, interestingly, the CO yield versus CO_2 conversion on the Ru/MgO catalysts with Ru loading from 0.5 to 1.0 wt.% adhered to the same linear relationship, suggesting that the CO yield was dominated by the CO_2 conversion. The 1.0Ru/MgO catalyst exhibited the highest CO_2 conversion at tested temperatures, resulting in the highest CO yield. It is evident that 1.0Ru/MgO featured the most active Ru sites, a conclusion further supported by the lower apparent activation energy (E_a) for CO_2 hydrogenation on this catalyst comparing to that on 0.5Ru/MgO (**Fig. 1e**). We also prepared a reference catalyst using MgO support directly (denoted as 1.0Ru/MgO-ref), and subjected to the CO_2 hydrogenation

testing. As shown in **Fig. S2**, higher CO_2 conversion and CO yield were observed on 1.0Ru/MgO catalyst prepared from $Mg(OH)_2$ support comparing to that on 1.0Ru/MgO-ref. This result suggests that loading Ru precursor on hydroxyl-rich $Mg(OH)_2$ followed by subsequent calcination could fabricate more beneficial structural configuration for the Ru active sites in catalytic CO_2 hydrogenation.

3.2. Structure characterization

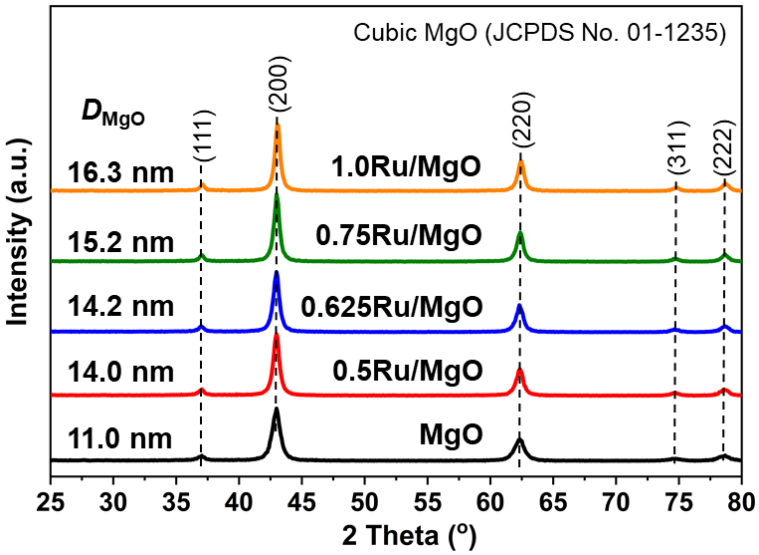

Fig. 3. Powder XRD patterns for the bare MgO, 0.5Ru/MgO, 0.625Ru/MgO, 0.75Ru/MgO, and 1.0Ru/MgO catalysts.

Fig. 3 shows the XRD patterns for the bare MgO and Ru/MgO catalysts. All diffraction peaks for the pristine MgO could be attributed to the cubic MgO crystal structure (JCPDS No. 01-1235). With the introduction of Ru, no additional diffraction peaks were observed for Ru/MgO catalysts, which should be due to the low Ru loading (≤ 1 wt.%) and the high dispersion of Ru species. To determine whether the introduction of Ru impacted the crystalline structure of MgO, the crystallite size of MgO (D_{MgO}) was calculated using the Scherer equation based on the full width at half maximum (FWHM) of the peak corresponding to the MgO(200) plane. As shown in **Fig. 3** and listed in **Table S1**, the increase of Ru loading led to a monotonic increase of the MgO crystallite size, for example, from 11.0 nm for MgO to 16.3 nm for 1.0Ru/MgO. These results suggest that the loading of Ru onto $Mg(OH)_2$, followed by calcination, accelerated the crystallization process of MgO. **Fig. S3a** illustrates the N_2 adsorption-desorption isotherms of MgO support and Ru/MgO

catalysts. All samples displayed characteristic type IV isotherms with distinct hysteresis loops (H3 type), suggesting the presence of mesopores.[34, 37] As shown in **Fig. S3b**, MgO exhibited a relatively well-defined mesopore size distribution ranging from 3 to 6 nm, while broader pore size distributions were observed for Ru/MgO catalysts extending up to 16 nm. As listed in **Table S1**, MgO showed the BET surface area of 119 m^2/g, the pore volume of 0.29 cm^3/g, and an average pore size of 5.4 nm. Upon the introduction of Ru, there was no noticeable impact on the pore volume, which remained in the range of 0.27 to 0.30 cm^3/g. However, there was a gradual decline in the BET surface area, decreasing from 119 to 92 m^2/g, and an increase in the average pore size from 5.4 to 8.5 nm. This decrease in surface area with increasing Ru loading could be attributed to the enhanced crystallization of MgO as verified by XRD results.

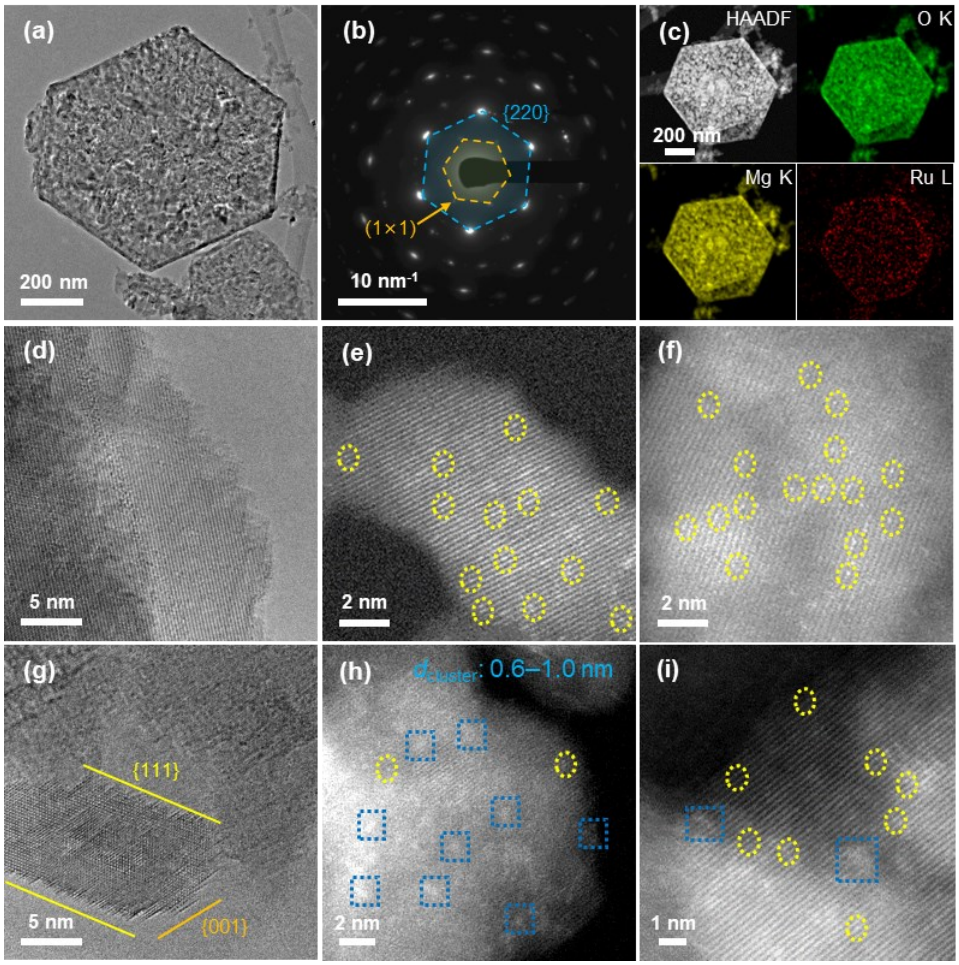

Fig. 4. (a) TEM image, (b) selected area electron diffraction (SAED), and (c) HAADF image and corresponding EDS elemental maps of 0.625Ru/MgO. (d, g) High-resolution TEM and (e, f, h, i) HAADF-STEM images of 0.5Ru/MgO (d-f) and 1.0Ru/MgO (g-i) catalysts.

TEM and STEM images were collected to determine the morphology and Ru structure of Ru/MgO catalysts. As depicted in **Fig. 4** and **Figs. S4-S8**, the Ru/MgO catalysts with varying Ru loadings exhibited consistent mesoporous nanoplate morphology. For instance, the 0.625Ru/MgO catalyst (**Fig. 4a-c** and **Fig. S5**), as exemplified here, displayed a single mesocrystalline nanoplate structure, with the majority of crystallites within the mesocrystal oriented along the 111-zone axis, perpendicular to the plate surface,[38] as confirmed by the selected area electron diffraction (SAED) results (**Fig. 4b**). EDS elemental mapping images (**Fig. 4c**) show that the Ru element was tracking well with O and Mg elements within this nanoplate, indicating a high dispersion of Ru species. Moreover, high-resolution TEM analysis demonstrated that the {111} surfaces of MgO were not atomically flat but rather structured by 001 nano-pyramidal textures (**Fig. 4g**); and these features were also discovered earlier in MgO thin films deposited by molecular beam epitaxy (MBE).[39] These non-atomically flat features could be beneficial for anchoring metal atoms. As expected, the Ru structures in the as-prepared Ru/MgO catalysts were confirmed to be Ru_1 or/and thin Ru clusters, with no obvious bulk Ru crystals observed. In the case of 0.5Ru/MgO catalyst, as shown in **Fig. 4d-f** and **Fig. S4**, exclusive Ru_1 was identified on the MgO support. As the Ru loading increased from 0.5 to 1.0 wt.%, in addition to the presence of Ru_1, Ru clusters in atomic-layer thickness with increased sizes also emerged on MgO. Specifically, the 0.625Ru/MgO (**Fig. S5**), 0.75Ru/MgO (**Fig. S6**), and 1.0Ru/MgO (**Fig. 4g-i** and **Fig. S7**) catalysts exhibited hybrid Ru structures, encompassing both Ru_1 and Ru clusters in atomic-layer thickness with sizes measuring < 0.3 nm, 0.2-0.4 nm, and 0.6-1.0 nm, respectively. With the further increase of Ru loading to 2.0 wt.%, bulk Ru particles were observed on 2.0Ru/MgO catalyst (**Fig. S8**), with sizes measuring 0.8-1.5 nm. The enlargement of the Ru cluster sizes could be attributed to the heightened Ru density on the MgO surface, which was a consequence of the decline in BET surface area and the increase in Ru loading. It was reported that the Ru particle sites benefited the CO_2 methanation pathway in CO_2 hydrogenation reaction.[27] The 2.0Ru/MgO catalyst, with the presence of bulk Ru particles, also facilitated the CO_2 methanation, resulting in the low CO selectivity and CO yield in CO_2 hydrogenation, as previously observed (**Fig. 1a-1b**; **Fig. S1b**).

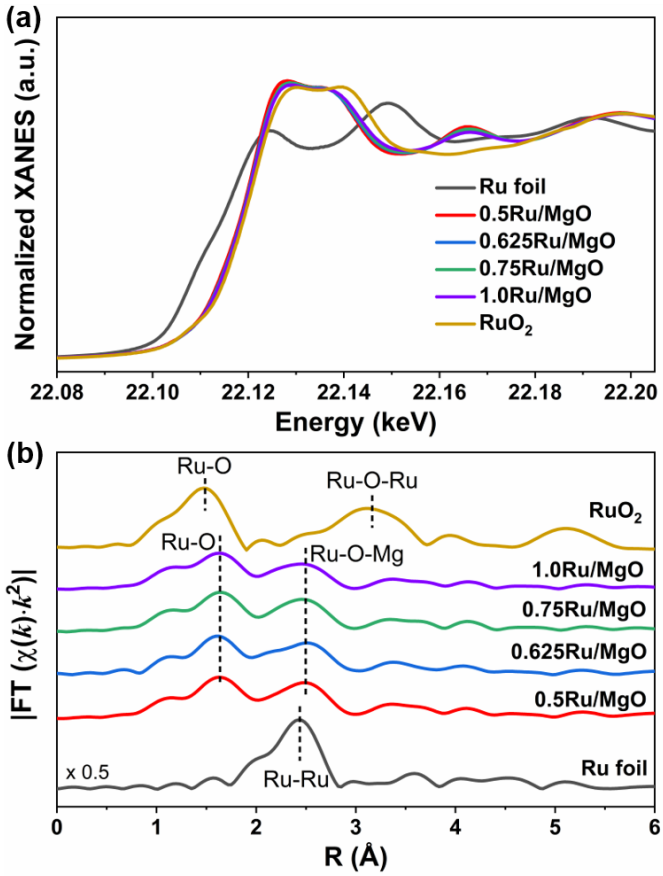

Fig. 5. (a) Normalized Ru K-edge XANES and (b) Fourier transformed k^2-weighted EXAFS oscillations in R space for Ru K-edge in 0.5Ru/MgO, 0.625Ru/MgO, 0.75Ru/MgO, and 1.0Ru/MgO catalysts.

XAS analysis was conducted to reveal the oxidation states and local coordination structure of Ru species on MgO. As illustrated in **Fig. 5a**, the white line intensity of Ru-K XANES for the Ru/MgO catalysts were very similar to that for RuO_2, indicating that the Ru species in these catalysts were in the form of oxide phase. According to the XANES linear combination fitting results (**Fig. S9**, **Table S2**), the averaged oxidation states of Ru species on the Ru/MgO catalysts were rather similar (3.7-3.8), which were close to that on RuO_2 reference (4.0). To further investigate the local coordination structure of Ru species, EXAFS curve fitting analysis was conducted. As demonstrated in **Fig. 5b**, for all the Ru/MgO catalysts, no Ru-Ru and Ru-O-Ru coordination shells were observed, indicating the absence of metallic Ru and RuO_2 particles. The exclusive presence of Ru-O and Ru-O-Mg coordination shells suggested that the Ru species in these catalysts were in the isolated or highly dispersed state. According to the EXAFS fitting

results (**Fig. S10**, **Table S3**), the coordination number (CN) of Ru-O and Ru-O-Mg on these Ru/MgO catalysts were similar, ranging from 5.4 to 6.0 and 10.0 to 12.0, respectively. The similar averaged Ru oxidation state and coordination environment suggest that the Ru species in these Ru/MgO catalysts showed similar local structures. When combined with the observations from TEM images which showed the presence of Ru clusters with atomic-layer thickness on the 0.625Ru/MgO, 0.75Ru/MgO, and 1.0Ru/MgO catalysts, it could be verified that the atomic single-layer (ASL) structures of Ru species with varying cluster sizes were created on MgO surface.

3.3. Reducibility and CO_2 adsorption properties

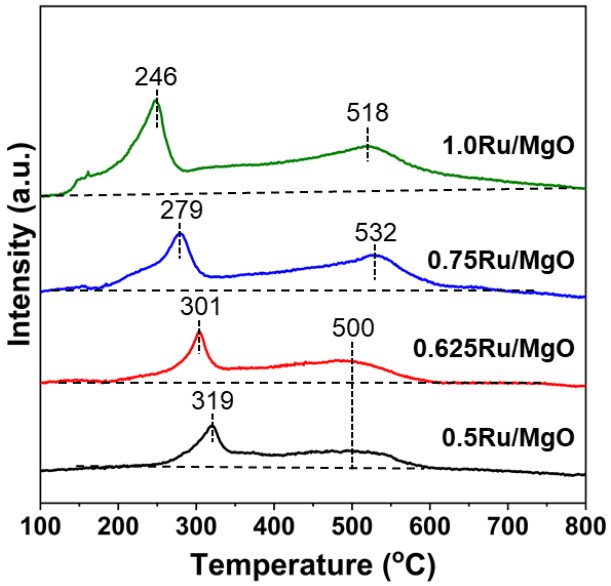

Fig. 6. H_2-TPR profiles for 0.5Ru/MgO, 0.625Ru/MgO, 0.75Ru/MgO, and 1.0Ru/MgO catalysts.

H_2-TPR experiments were conducted to investigate the reducibility of the Ru/MgO catalysts. As shown in **Fig. 6**, two distinct reduction peaks were observed for all catalysts. The first peak centered at 246-319 °C could be assigned to the reduction of highly dispersed RuO_x species, while the second peak at 500-532 °C was associated with the reduction of RuO_x species strongly bound with MgO.[16, 34, 40] With the increase of Ru loading, a noticeable shift in the first reduction peak for the highly dispersed RuO_x species to lower temperature was observed, indicating the improved ability to dissociate H_2. The amount of H_2 consumptions were further quantified and are presented in **Table 1**. With the elevated Ru loading, a substantial increase in the total H_2 consumption was observed, from 14.8 μmol/g_{cat} for 0.5Ru/MgO to 35.6 μmol/g_{cat} for 1.0Ru/MgO.

339 As verified by the STEM images, the presence of more Ru_{ASL} was observed with the increased Ru
340 loading within Ru/MgO catalysts, which probably resulted in the improved low-temperature
341 reducibility and, consequently, enhanced H_2 dissociation. Such enhanced ability to dissociate H_2
342 on the Ru/MgO catalysts with higher Ru loading should be accountable for the improved CO_2
343 hydrogenation activity and the decreased CO selectivity, as observed in **Fig. 1**.

344 **Table 1**. H_2 consumption and CO_2 adsorption on the bare MgO and Ru/MgO catalysts.

Samples	H_2 consumption ($\mu mol/g_{cat}$)[a]	CO_2 adsorption ($\mu mol\ CO_2/m^2$)[b]	
		1st peak	Total
MgO	-	-	2.25
0.5Ru/MgO	14.8	0.08	3.21
0.625Ru/MgO	15.6	0.09	3.35
0.75Ru/MgO	28.9	0.16	4.45
1.0Ru/MgO	35.6	0.29	3.90

345 [a] Calculated based on the H_2-TPR results using a standard CuO sample as reference.

346 [b] Calculated based on the CO_2-TPD results, normalized by BET surface areas. The 1st peak in CO_2-
347 TPD is for the CO_2 desorption from the Ru-MgO interface.

348 To demonstrate the CO_2 adsorption capacity, CO_2-TPD experiments were conducted and the
349 results are presented in **Fig. 7**. Consistent with prior reports,[32, 41, 42] three distinct CO_2
350 desorption peaks were observed on bare MgO support. These peaks corresponded to the
351 decomposition of bicarbonate species at 167 °C formed through reaction between CO_2 and
352 hydroxyl groups, bidentate carbonate species at 248 °C, and monodentate carbonate species at
353 438 °C. Upon loading Ru onto MgO, an additional CO_2 desorption peak at 118-121 °C emerged,
354 which probably could be assigned to the decomposition of bicarbonate species formed at the Ru-
355 MgO interface. In addition, the decomposition temperatures for bicarbonate species at the Ru-
356 MgO interface and on the MgO surface reduced as the Ru loading increased, indicating that the
357 presence of Ru species enhanced the decomposition of bicarbonate species. It is noteworthy that
358 the CO_2 desorption persisted up to a temperature of 600 °C, suggesting the superior stability of

these adsorbed CO_2 species. This stability allows these adsorbed CO_2 species to actively participate in CO_2 hydrogenation at the operational reaction temperatures. By integrating the peak areas obtained from CO_2-TPD, the amount of CO_2 desorption was calculated and normalized by the BET surface areas. As summarized in **Table 1**, the amount of CO_2 desorbed from the Ru-MgO interface increased with the elevation of Ru loading, ranging from 0.08 to 0.29 μmol CO_2/m^2. In comparison to the total CO_2 desorption of 2.25 μmol CO_2/m^2 on the pristine MgO surface, much higher CO_2 desorption ranging from 3.21 to 4.45 μmol CO_2/m^2 on the Ru/MgO catalysts was observed, which suggested that the Ru-MgO interface played an important role in enhancing CO_2 adsorption. The improved CO_2 adsorption capacity might also effectively facilitate the CO_2 hydrogenation process.

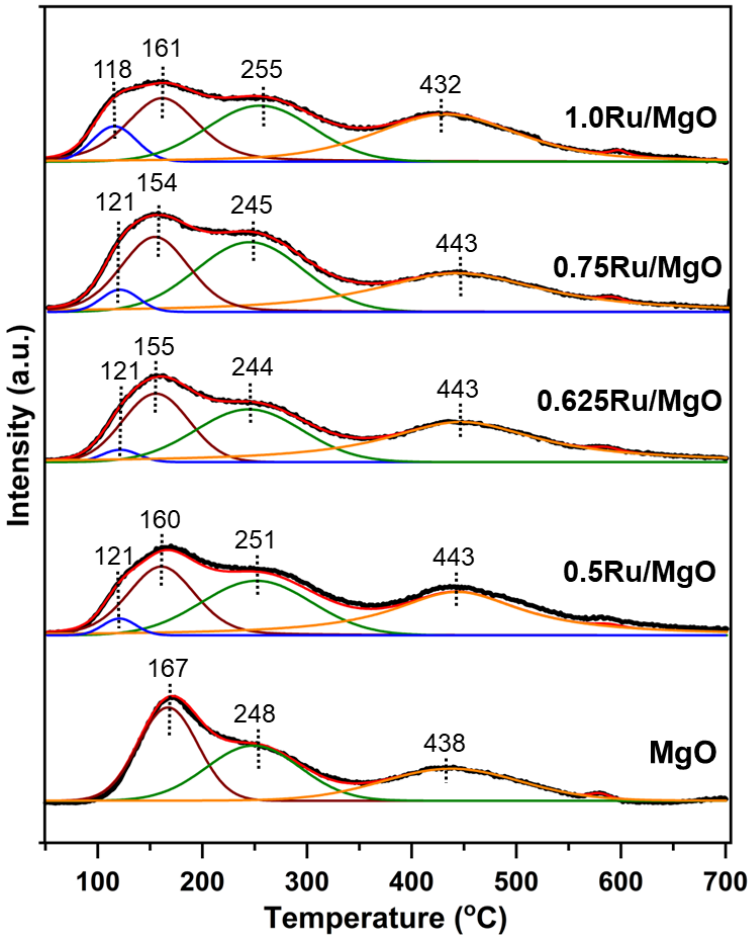

Fig. 7. CO_2-TPD profiles on bare MgO, 0.5Ru/MgO, 0.625Ru/MgO, 0.75Ru/MgO, and 1.0Ru/MgO catalysts.

In situ DRIFTS of CO_2 adsorption were performed on the 0.5Ru/MgO and 1.0Ru/MgO catalysts to determine the effect of Ru structures on CO_2 adsorption behavior. As depicted in **Fig. S11**, upon the exposure to CO_2, distinct adsorption peaks appeared and reached stable state on both catalysts within *ca.* 10 min. The peaks observed at 1222, 1281 cm^{-1}, and 1624/1643 cm^{-1} could be attributed to bicarbonate species.[34, 43] Additionally, the peaks at 1547 and 1378/1362 cm^{-1} were indicative of monodentate carbonate species, and the peaks at 1501, 1667, and 1693/1688 cm^{-1} corresponded to bidentate carbonate species.[44] Consistent with the findings from CO_2-TPD, more pronounced CO_2 adsorption peaks were observed on 1.0Ru/MgO comparing to those on 0.5Ru/MgO, again affirming the promotion effect of Ru species on MgO for CO_2 adsorption. In addition, more abundant bidentate carbonate species were observed on 1.0Ru/MgO, indicating that the bidentate carbonate species preferred to form at the interface between Ru_{ASL} and MgO support.

3.4. Catalytic stability

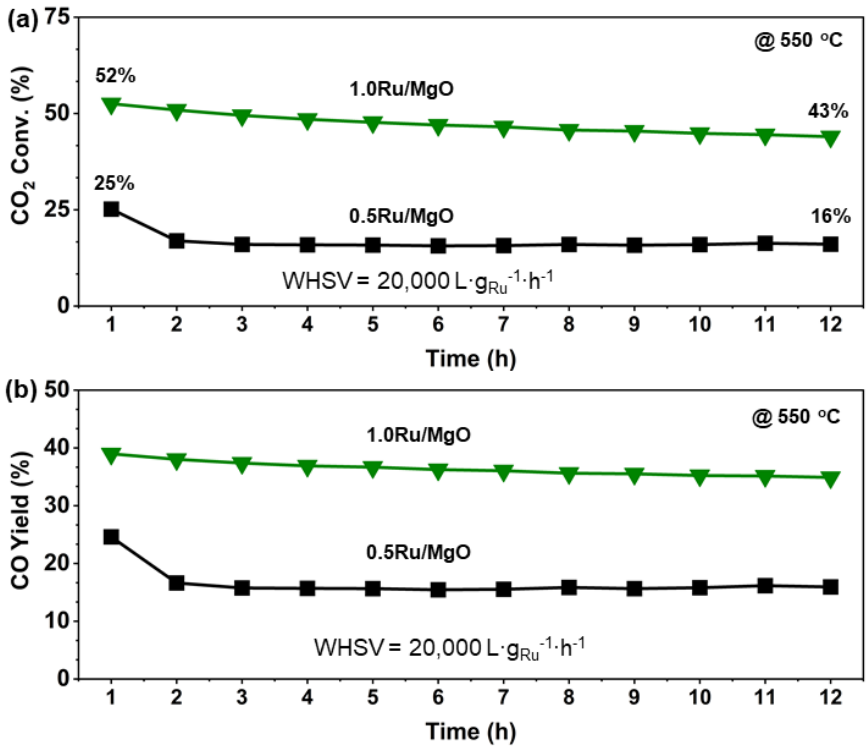

Fig. 8. On-stream (a) CO_2 conversion and (b) CO yield at 550 °C on 0.5Ru/MgO and 1.0Ru/MgO catalysts under a WHSV of 20,000 $L \cdot g_{Ru}^{-1} \cdot h^{-1}$.

The catalytic stability of 0.5Ru/MgO and 1.0Ru/MgO catalysts for CO_2 hydrogenation was assessed at 550 °C for 12 h, operated under the WHSV of 20,000 $L \cdot g_{Ru}^{-1} \cdot h^{-1}$. As illustrated in **Fig.**

8, both catalysts exhibited a slightly decline in CO_2 conversion and CO yield during the testing. However, even after 12 h operation, the CO_2 conversion of 43% on 1.0Ru/MgO was still 2.7 times of that of 16% on 0.5Ru/MgO. This observation suggests that the Ru_{ASL} sites in the 1.0Ru/MgO catalyst exhibited much higher intrinsic activity comparing to the Ru_1 sites in the 0.5Ru/MgO catalyst.

To gain insights into the factors contributing to the catalyst deactivation, XRD patterns and HAADF-STEM images of the post-reaction catalysts (after CO_2 hydrogenation testing at 550 °C for 12 h), denoted as 0.5Ru/MgO-*p* and 1.0Ru/MgO-*p*, were collected. **Fig. S12** presents the XRD patterns of the 0.5Ru/MgO, 1.0Ru/MgO, 0.5Ru/MgO-*p*, and 1.0Ru/MgO-*p* catalysts. No detectable additional species were observed on 0.5Ru/MgO-*p* and 1.0Ru/MgO-*p*, aside from cubic MgO. However, a slight increase in the crystallite size of MgO was observed for both 0.5Ru/MgO (from 14.0 to 16.7 nm) and 1.0Ru/MgO (from 16.3 to 18.5 nm) after the reaction. **Fig. 9** presents the HAADF images for the 0.5Ru/MgO-*p* and 1.0Ru/MgO-*p* catalysts. Notably, alongside the presence of Ru_1 in 0.5Ru/MgO-*p*, and both Ru_1 and Ru_{ASL} in 1.0Ru/MgO-*p*, Ru nanoparticles appeared on both catalysts as well. The formation of a portion of Ru nanoparticles in both catalysts, resulting from the sintering of Ru single atoms or/and small Ru clusters, should have contributed to the deactivation of the Ru/MgO catalysts after CO_2 hydrogenation at 550 °C for 12 h.

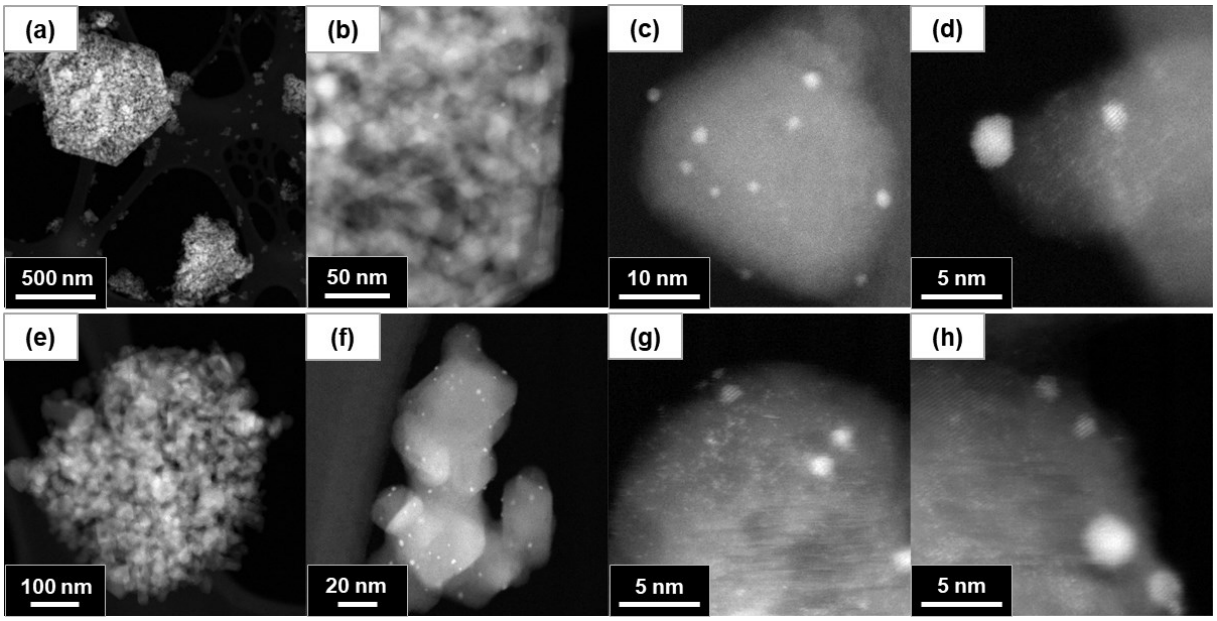

Fig. 9. HAADF images for (a−d) 0.5Ru/MgO-*p* and (e−h) 1.0Ru/MgO-*p* catalysts.

The XANES and EXAFS of Ru K-edge were also measured to elucidate the oxidation states and local structures of Ru species within the 0.5Ru/MgO-*p* and 1.0Ru/MgO-*p* catalysts. As depicted in **Fig. S13a**, the white line intensity and absorption edge energy of Ru K-edge XANES for the 0.5Ru/MgO and 1.0Ru/MgO catalysts decreased after on-stream CO_2 hydrogenation at 550 °C for 12 h, suggesting a decreased oxidation state of Ru species within 0.5Ru/MgO-*p* and 1.0Ru/MgO-*p*. This observation was confirmed by the XANES linear combination fitting results (**Fig. S14** and **Table S2**), where the averaged Ru oxidation state declined from 3.8 to 2.9 in 0.5Ru/MgO and from 3.8 to 2.5 in 1.0Ru/MgO, respectively, with a more pronounced decrease in the latter one. As revealed by the EXAFS curve fitting results (**Table S3** and **Figs. S13b** and **S15**), besides Ru-O and Ru-O-Mg bonds, the presence of Ru-Ru bonds was also observed in the 0.5Ru/MgO-*p* and 1.0Ru/MgO-*p* catalysts, confirming the formation of metallic Ru nanoparticles. The 1.0Ru/MgO-*p* catalyst exhibited lower CNs of Ru-O (5.4 *vs.* 6.4) and Ru-O-Mg (7.0 *vs.* 11.0) but a slightly higher CN of Ru-Ru (5.4 *vs.* 4.8) comparing to the 0.5Ru/MgO-*p* catalyst. These results suggest that slghtly larger Ru nanoparticles were formed on the 1.0Ru/MgO-*p* after the long-term activity testing at 550 °C because of the relatively higher surface density of Ru species including both Ru_1 and Ru_{ASL} structures.

3.5. CO_2 hydrogenation mechanism on Ru/MgO

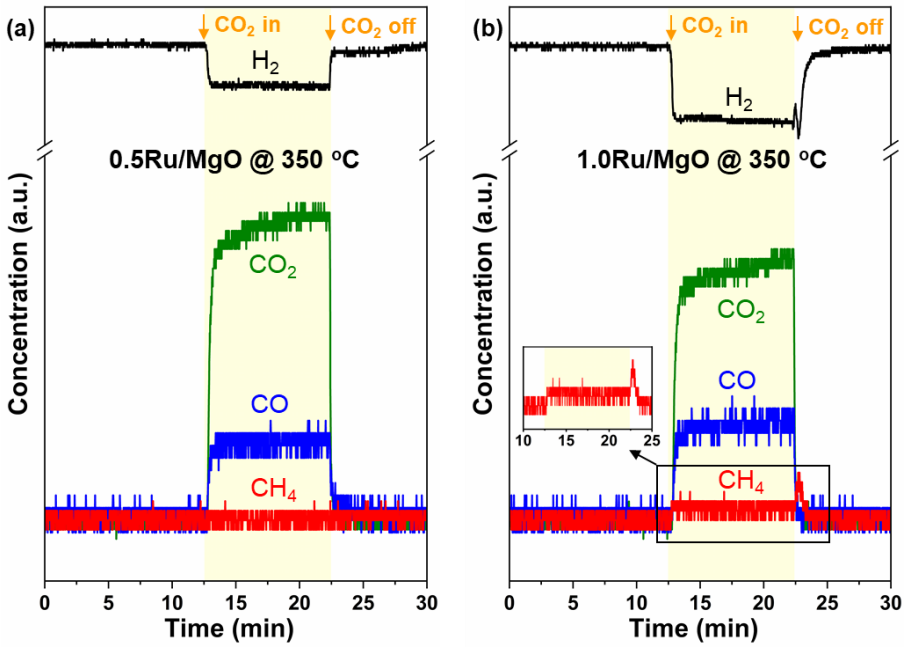

Fig. 10. Transient CO_2 hydrogenation performance as a function of time on (a) 0.5Ru/MgO and

(b) 1.0Ru/MgO catalysts at 350 °C. Note: Prior to the test, the loaded catalyst was pretreated in RWGS reaction flow at 500 °C for 30 min and then cooled down to 350 °C. Following the transition to 10% H_2/Ar flow (40 mL·min^{-1}) for 12.5 min, 2.5% CO_2 was introduced and maintained for 10 min, after which the CO_2 flow was subsequently cut off.

To investigate the CO_2 hydrogenation mechanism on Ru_1 and Ru_{ASL}, transient CO_2 hydrogenation tests on 0.5Ru/MgO and 1.0Ru/MgO catalysts were conducted at the temperature of 350 °C. As depicted in **Fig. 10a**, when CO_2 was introduced into the H_2 flow over the 0.5Ru/MgO catalyst, a decrease in H_2 concentration was observed along with the emergence of CO formation, with no CH_4 formation detected. On the 1.0Ru/MgO catalyst (**Fig. 10b**), in clear contrast, a more substantial decrease in H_2 concentration, a much lower CO_2 concentration, and a higher level of CO formation were observed. Notably, CH_4 formation over the 1.0Ru/MgO catalyst was also detected, especially when the CO_2 supply was discontinued. Consistent with the results of CO_2 hydrogenation, these findings suggest that the 1.0Ru/MgO catalyst containing both Ru_1 and Ru_{ASL} sites exhibit higher CO_2 hydrogenation activity but relatively lower CO selectivity when comparing to the 0.5Ru/MgO catalyst with only Ru_1 sites. The immediate bump of CH_4 concentration upon CO_2 cut-off suggests that the adsorbed CO_2 species might play a more important role in CH_4 formation than gas-phase CO_2 on 1.0Ru/MgO.

To investigate the behavior of Ru active sites in CO_2 hydrogenation, *in situ* XANES analysis of the Ru K-edge in 0.5Ru/MgO and 1.0Ru/MgO catalysts under varying testing conditions was performed. The results, as shown in **Fig. 11**, revealed a similar trend in the changes of the white line intensities and the average Ru oxidation states for both 0.5Ru/MgO and 1.0Ru/MgO during the different testing steps. At 30 °C, when transitioning from Ar flow (Step 1) to reaction flow (CO_2 + H_2) (Step 2), no significant alteration in Ru oxidation state was observed for catalysts. Upon increasing the temperature to 500 °C in the same reaction flow (Step 3), the Ru oxidation state decreased on both catalysts. A more pronounced decline was noted on 1.0Ru/MgO (from 3.6 to 3.1) compared to that on 0.5Ru/MgO (from 3.8 to 3.5). This discrepancy might be attributed to the more efficient H_2 activation on Ru_{ASL} sites within 1.0Ru/MgO, leading to a more significant reduction of Ru species. At 500 °C, whether transitioning the reaction flow to CO_2 flow (Step 4) or switching back to the reaction flow (Step 5), no substantial change in the Ru oxidation state was observed. These findings suggest that the partially reduced Ru species on MgO support remained

stable and were unable to be re-oxidized by CO_2. In other words, the Ru species in these catalysts only functioned as active sites for H_2 dissociation during the CO_2 hydrogenation rather than serving as redox active sites to activate CO_2. In CO_2 hydrogenation, the gas-phase CO_2 or adsorbed CO_2 species on MgO could be directly reduced by dissociated H on Ru sites or at the interfaces between Ru and MgO. Upon cooling down the samples to 30 °C in the reaction flow (Step 6), the Ru oxidation state returned to the initial status for 0.5Ru/MgO (3.7), whereas it did not fully recover for 1.0Ru/MgO (3.2). These results suggest that the changes in partial Ru species on 1.0Ru/MgO were irreversible, likely due to the formation of metallic Ru clusters with relatively larger size.

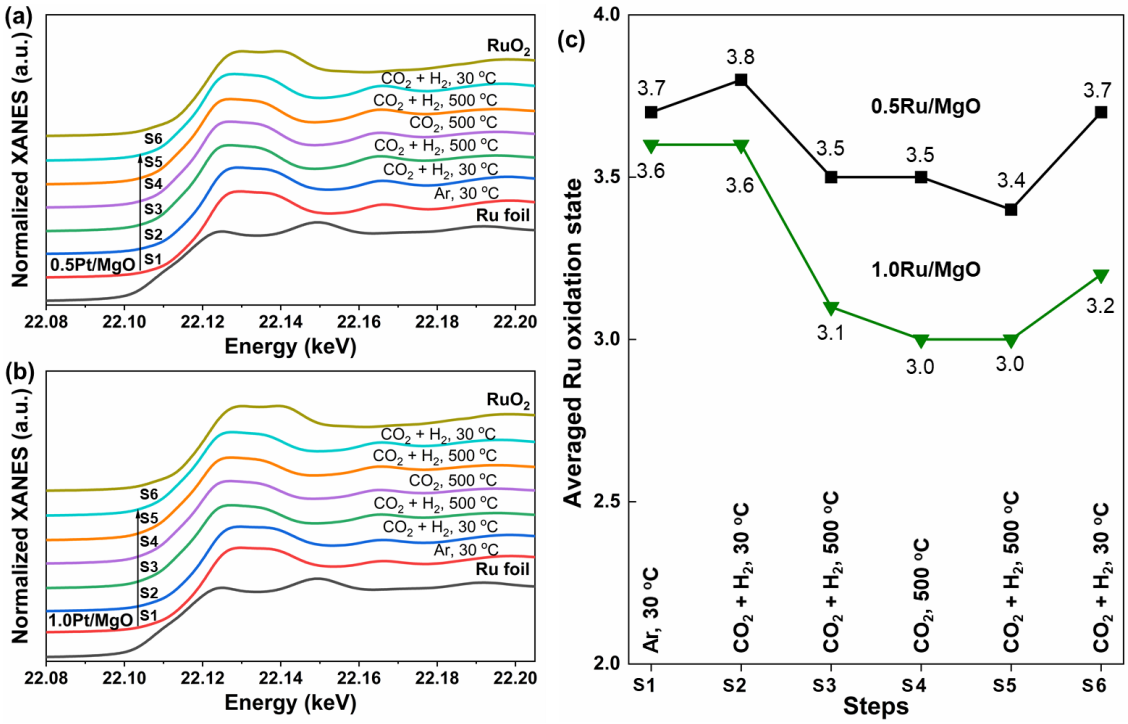

Fig. 11. *In situ* XANES of Ru K-edge in (a) 0.5Ru/MgO and (b) 1.0Ru/MgO catalysts, as well as their corresponding (c) averaged Ru oxidation states under different testing conditions. S1-S6 suggest the different experimental steps with varied reaction atmosphere and temperatures. The averaged Ru oxidation states were determined by the linear combination fitting of Ru K-edge XANES using Ru foil and RuO_2 as references.

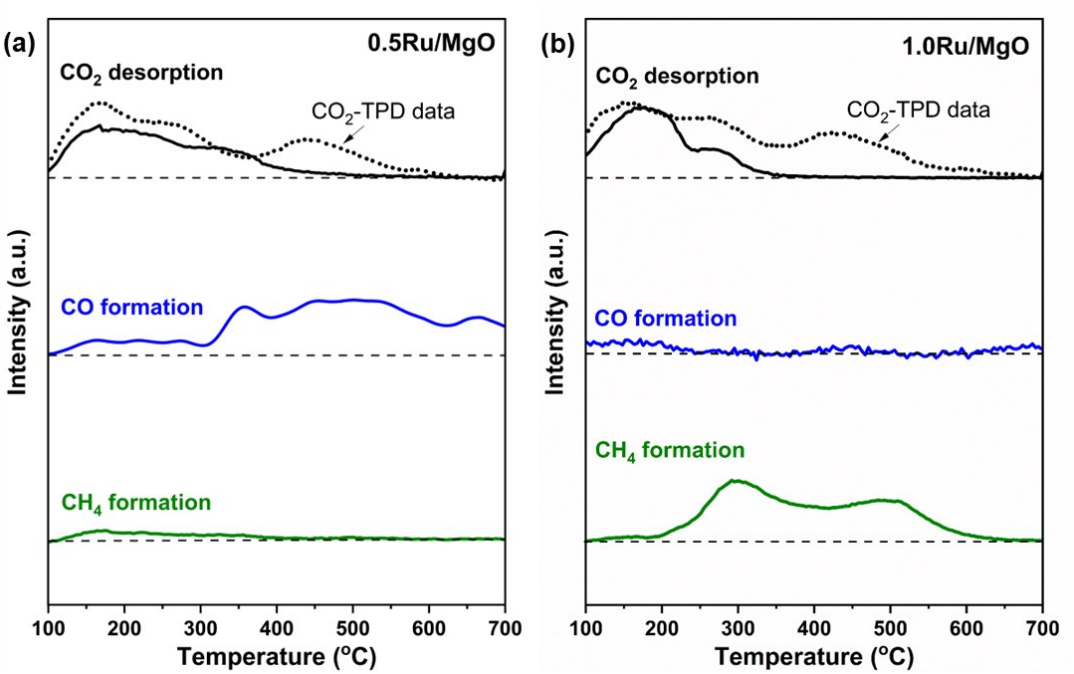

Fig. 12. CO_2 desorption, CO formation, and CH_4 formation during H_2-TPSR experiments on (a) 0.5Ru/MgO and (b) 1.0Ru/MgO catalysts. The dotted curves are the CO_2 desorption data obtained from CO_2-TPD experiments.

To verify whether adsorbed CO_2 species participated in the CO_2 hydrogenation reaction, H_2-TPSR experiments were conducted by flowing H_2 to the catalysts with pre-adsorbed CO_2 species. **Fig. 12** shows the CO_2 desorption, CO formation, and CH_4 formation during the H_2-TPSR tests on 0.5Ru/MgO and 1.0Ru/MgO catalysts. Comparing to the CO_2 desorption from CO_2-TPD, significantly lower CO_2 desorption was observed during the H_2-TPSR process. This clearly suggests the consumption of partial adsorbed CO_2 species through the hydrogenation reaction. On the 0.5Ru/MgO catalyst, as shown in **Fig. 12a**, the consumption of CO_2 from bicarbonate and bidentate carbonate species at lower temperatures (below 350 °C) resulted in the formation of both CO and CH_4, while the consumption of CO_2 from monodentate carbonate species at higher temperatures (above 350 °C) led primarily to the formation of CO. In contrast, on the 1.0Ru/MgO catalyst (**Fig. 12b**), the consumption of CO_2 from bicarbonate species resulted in the production of CO, while the significant consumption of bidentate and monodentate carbonate species led to the formation of CH_4. These results confirmed that the adsorbed CO_2 species were able to participate in the CO_2 hydrogenation reaction. However, distinct CO_2 hydrogenation pathways were followed on different Ru sites: the hydrogenation of adsorbed CO_2 species followed the

RWGS pathway on Ru_1 sites, as indicated by the dominant production of CO; conversely, it followed the CO_2 methanation pathway on Ru_{ASL} sites with CH_4 being the dominant product. These findings aligned well with the results obtained from the CO_2 hydrogenation experiments and the transient CO_2 hydrogenation tests, reinforcing the conclusion that the 1.0Ru/MgO catalyst containing both Ru_1 and Ru_{ASL} sites exhibited relatively lower CO selectivity than the 0.5Ru/MgO catalyst. This result could be effectively explained by the enhanced H_2 dissociation capability of Ru_{ASL} sites and the presence of reactive bidentate and monodentate carbonate species at the Ru-MgO interface, which together facilitated the CO_2 methanation reaction to produce CH_4 to a certain extent.

4. Conclusions

Ru/MgO catalysts were prepared with Ru in the form of single atoms or a combination of single atoms and Ru clusters/nanoparticles, achieved by varying Ru loading in the range of 0.5-2.0 wt.% and employing the commercial $Mg(OH)_2$ as support. In the context of CO_2 hydrogenation, the 0.5Ru/MgO catalyst, containing only Ru single atoms (Ru_1), exhibited lower CO_2 conversion while maintaining 100% CO selectivity. As the Ru loading increased, more Ru clusters formed within the Ru/MgO catalysts, leading to the enhanced CO_2 conversion but a decrease in CO selectivity. Among all studied catalysts, the 1.0Ru/MgO catalyst, featuring both Ru_1 and atomic single-layer Ru cluster (Ru_{ASL}) with the size of 0.6-1.0 nm, demonstrated the highest CO yield by achieving a balanced CO_2 conversion and CO selectivity. As confirmed by H_2-TPR results, the presence of Ru_{ASL} facilitated the H_2 dissociation. With the increase of Ru loading, more Ru-MgO interfaces were generated, resulting in the improved CO_2 adsorption capacity, as determined by CO_2-TPD and *in situ* DRIFTS of CO_2 adsorption. Additionally, the CO_2 hydrogenation pathways on the 0.5Ru/MgO and 1.0Ru/MgO catalysts were investigated through the transient CO_2 hydrogenation tests and H_2-TPSR experiments, which demonstrated the involvement of adsorbed CO_2 species in CO_2 hydrogenation. On Ru_1 sites, CO_2 hydrogenation followed the reverse water-gas shift (RWGS) pathway, resulting in the production of CO. In contrast, on Ru_{ASL} sites, the enhanced H_2 dissociation ability, along with the presence of adsorbed bidentate and monodentate carbonate species at the Ru-MgO interface, facilitated the formation of CH_4 through the CO_2 methanation pathway. As a consequence, a composite structure comprising Ru_1 and Ru_{ASL} on MgO should be favored for the CO_2 hydrogenation reaction to efficiently generate the value-added CO. This work underscores the significant impact of the structure and local environment of Ru species

in Ru/MgO catalysts on the CO_2 hydrogenation pathways. Through the fine tuning of Ru structures, one can direct the reaction into distinct pathways, offering a critical handle to regulate catalyst efficiency and selectivity. This study provides new insights in the development of selective catalysts in essential chemical reactions.

CRediT authorship contribution statement

Shaohua Xie: Investigation, Writing – original draft, Writing – review & editing, Visualization. **Kailong Ye**: Investigation, Formal analysis, Visualization. **Jingshan S. Du**: Investigation, Resources, Writing – review & editing. **Xing Zhang**: Investigation. **Daekun Kim**: Investigation. **Jeremia Loukusa**: Investigation. **Lu Ma**: Investigation, Resources. **Steven N. Ehrlich**: Investigation, Resources. **Nebojsa S. Marinkovic**: Investigation, Resources. **James J. De Yoreo**: Investigation, Resources, Writing – review & editing. **Fudong Liu**: Supervision, Methodology, Investigation, Funding acquisition, Writing – review & editing.

Declaration of Competing Interest

The authors declare that they have no known competing financial interests or personal relationships that could have appeared to influence the work reported in this paper.

Data availability

The data supporting the findings of this study are available in the main text and supplementary information files. Additional data are available upon reasonable request from the corresponding author.

Acknowledgment

This work was supported by the National Science Foundation (NSF) grant (CHE-1955343), the NSF-PREM grant (DMR-2121953), and the Startup Fund (F.L.) from the University of Central Florida (UCF) and the University of California, Riverside (UCR). S.X., X.Z., and D.K. thank the support from the Preeminent Postdoctoral Program (P3) at the University of Central Florida (UCF). J.J.D.Y. acknowledges the support from the University of Washington Molecular Engineering Materials Center (MEM-C), a NSF Materials Research Science and Engineering Center (DMR-1719797). J.S.D. acknowledges a Washington Research Foundation Postdoctoral Fellowship. This

research used beamline 7-BM (QAS) of the National Synchrotron Light Source II (NSLS-II), a U.S. Department of Energy (DOE) Office of Science User Facility operated for the DOE Office of Science by Brookhaven National Laboratory (BNL) under Contract No. DE-SC0012704. Beamline operations were supported in part by the Synchrotron Catalysis Consortium, U.S. DOE, Office of Basic Energy Sciences (Grant No. DE-SC0012335). This study made use of electron microscopy facilities at Pacific Northwest National Laboratory (PNNL), including user facilities at the Environmental Molecular Sciences Laboratory. PNNL is a multi-program national laboratory operated for DOE by Battelle under Contract No. DE-AC05-76RL01830.

Appendix A. Supplementary data

Supplementary data to this article can be found online at https://doi.org/10.1016/j.cej.2023.xxxxxx.

References

[1] M.D. Porosoff, B. Yan, J.G. Chen, Catalytic reduction of CO_2 by H_2 for synthesis of CO, methanol and hydrocarbons: challenges and opportunities, Energ. Environ. Sci. 9 (2016) 62-73.

[2] H.C. Wu, Y.C. Chang, J.H. Wu, J.H. Lin, I.K. Lin, C.S. Chen, Methanation of CO_2 and reverse water gas shift reactions on Ni/SiO_2 catalysts: the influence of particle size on selectivity and reaction pathway, Catal. Sci. Technol. 5 (2015) 4154-4163.

[3] W. Wang, S. Wang, X. Ma, J. Gong, Recent advances in catalytic hydrogenation of carbon dioxide, Chem. Soc. Rev. 40 (2011) 3703-3727.

[4] T. Abe, M. Tanizawa, K. Watanabe, A. Taguchi, CO_2 methanation property of Ru nanoparticle-loaded TiO_2 prepared by a polygonal barrel-sputtering method, Energ. Environ. Sci. 2 (2009) 315-321.

[5] F. Wang, S. He, H. Chen, B. Wang, L. Zheng, M. Wei, D.G. Evans, X. Duan, Active Site Dependent Reaction Mechanism over Ru/CeO_2 Catalyst toward CO_2 Methanation, J. Am. Chem. Soc. 138 (2016) 6298-6305.

[6] E. Pahija, C. Panaritis, S. Gusarov, J. Shadbahr, F. Bensebaa, G. Patience, D.C. Boffito, Experimental and Computational Synergistic Design of Cu and Fe Catalysts for the Reverse Water–Gas Shift: A Review, ACS Catal. 12 (2022) 6887-6905.

[7] A.M. Bahmanpour, M. Signorile, O. Kröcher, Recent progress in syngas production via catalytic CO_2 hydrogenation reaction, Appl. Catal. B: Environ. 295 (2021) 120319.

[8] V. Jiménez, P. Sánchez, P. Panagiotopoulou, J.L. Valverde, A. Romero, Methanation of CO, CO_2 and selective methanation of CO, in mixtures of CO and CO_2, over ruthenium carbon nanofibers catalysts, Appl. Catal. A: Gen. 390 (2010) 35-44.

[9] W.K. Fan, M. Tahir, Recent trends in developments of active metals and heterogenous materials for catalytic CO_2 hydrogenation to renewable methane: A review, J. Environ. Chem. Eng. 9 (2021) 105460.

[10] Y. Zhuang, R. Currie, K.B. McAuley, D.S.A. Simakov, Highly-selective CO_2 conversion via reverse water gas shift reaction over the 0.5wt% Ru-promoted Cu/ZnO/Al_2O_3 catalyst, Appl. Catal. A: Gen. 575 (2019) 74-86.

[11] A.I.M. Rabee, D. Zhao, S. Cisneros, C.R. Kreyenschulte, V. Kondratenko, S. Bartling, C. Kubis, E.V. Kondratenko, A. Brückner, J. Rabeah, Role of interfacial oxygen vacancies in low-loaded Au-based catalysts for the low-temperature reverse water gas shift reaction, Appl. Catal. B:

Environ. 321 (2023) 122083.
[12] Z. Zhao, M. Wang, P. Ma, Y. Zheng, J. Chen, H. Li, X. Zhang, K. Zheng, Q. Kuang, Z.-X. Xie, Atomically dispersed Pt/CeO_2 catalyst with superior CO selectivity in reverse water gas shift reaction, Appl. Catal. B: Environ. 291 (2021) 120101.
[13] S. Kattel, P. Liu, J.G. Chen, Tuning selectivity of CO_2 hydrogenation reactions at the metal/oxide interface, J. Am. Chem. Soc. 139 (2017) 9739-9754.
[14] J. Graciani, K. Mudiyanselage, F. Xu, A.E. Baber, J. Evans, S.D. Senanayake, D.J. Stacchiola, P. Liu, J. Hrbek, J. Fernández Sanz, J.A. Rodriguez, Highly active copper-ceria and copper-ceria-titania catalysts for methanol synthesis from CO_2, Science 345 (2014) 6196.
[15] Z. Hao, J. Shen, S. Lin, X. Han, X. Chang, J. Liu, M. Li, X. Ma, Decoupling the effect of Ni particle size and surface oxygen deficiencies in CO_2 methanation over ceria supported Ni, Appl. Catal. B: Environ. 286 (2021) 119922.
[16] C. Wang, Y. Lu, Y. Zhang, H. Fu, S. Sun, F. Li, Z. Duan, Z. Liu, C. Wu, Y. Wang, H. Sun, Z. Yan, Ru-based catalysts for efficient CO_2 methanation: Synergistic catalysis between oxygen vacancies and basic sites, Nano Research (2023) doi.org/10.1007/s12274-023-5592-3.
[17] T. Avanesian, G.S. Gusmão, P. Christopher, Mechanism of CO_2 reduction by H_2 on Ru(0 0 0 1) and general selectivity descriptors for late-transition metal catalysts, J. Catal. 343 (2016) 86-96.
[18] N. Sathishkumar, S.Y. Wu, H.T. Chen, Mechanistic insights into chemical reduction of CO_2 by reverse water-gas shift reaction on Ru(0001) surface: The water promotion effect, Appl. Surf. Sci. 581 (2022) 152354.
[19] A. Kim, C. Sanchez, G. Patriarche, O. Ersen, S. Moldovan, A. Wisnet, C. Sassoye, D.P. Debecker, Selective CO_2 methanation on Ru/TiO_2 catalysts: unravelling the decisive role of the TiO_2 support crystal structure, Catal. Sci. Technol. 6 (2016) 8117-8128.
[20] G. Garbarino, D. Bellotti, E. Finocchio, L. Magistri, G. Busca, Methanation of carbon dioxide on Ru/Al_2O_3: Catalytic activity and infrared study, Catal. Today 277 (2016) 21-28.
[21] A. Quindimil, U. De-La-Torre, B. Pereda-Ayo, A. Davó-Quiñonero, E. Bailón-García, D. Lozano-Castelló, J.A. González-Marcos, A. Bueno-López, J.R. González-Velasco, Effect of metal loading on the CO_2 methanation: A comparison between alumina supported Ni and Ru catalysts, Catal. Today 356 (2020) 419-432.
[22] J. Xu, X. Su, H. Duan, B. Hou, Q. Lin, X. Liu, X. Pan, G. Pei, H. Geng, Y. Huang, T. Zhang, Influence of pretreatment temperature on catalytic performance of rutile TiO_2-supported

ruthenium catalyst in CO_2 methanation, J. Catal. 333 (2016) 227-237.
[23] J. Zhou, Z. Gao, G. Xiang, T. Zhai, Z. Liu, W. Zhao, X. Liang, L. Wang, Interfacial compatibility critically controls Ru/TiO_2 metal-support interaction modes in CO_2 hydrogenation, Nat. Commun. 13 (2022) 327.
[24] A. Aitbekova, L. Wu, C.J. Wrasman, A. Boubnov, A.S. Hoffman, E.D. Goodman, S.R. Bare, M. Cargnello, Low-temperature restructuring of CeO_2-supported Ru nanoparticles determines selectivity in CO_2 catalytic reduction, J. Am. Chem. Soc. 140 (2018) 13736-13745.
[25] H. Xin, L. Lin, R. Li, D. Li, T. Song, R. Mu, Q. Fu, X. Bao, Overturning CO_2 hydrogenation selectivity with high activity via reaction-induced strong metal-support interactions, J. Am. Chem. Soc. 144 (2022) 4874-4882.
[26] R. Tang, Z. Zhu, C. Li, M. Xiao, Z. Wu, D. Zhang, C. Zhang, Y. Xiao, M. Chu, A. Genest, G. Rupprechter, L. Zhang, X. Zhang, L. He, Ru-catalyzed reverse water gas shift reaction with near-unity selectivity and superior stability, ACS Mater. Lett. 3 (2021) 1652-1659.
[27] J.H. Kwak, L. Kovarik, J. Szanyi, CO_2 reduction on supported Ru/Al_2O_3 catalysts: Cluster size dependence of product selectivity, ACS Catal. 3 (2013) 2449-2455.
[28] Y. Guo, S. Mei, K. Yuan, D.J. Wang, H.C. Liu, C.H. Yan, Y.W. Zhang, Low-temperature CO_2 methanation over CeO_2-supported Ru single atoms, nanoclusters, and nanoparticles competitively tuned by strong metal–support interactions and H-spillover effect, ACS Catal. 8 (2018) 6203-6215.
[29] F. Wang, C. Li, X. Zhang, M. Wei, D.G. Evans, X. Duan, Catalytic behavior of supported Ru nanoparticles on the {1 0 0}, {1 1 0}, and {1 1 1} facet of CeO_2, J. Catal. 329 (2015) 177-186.
[30] S. Sharma, Z. Hu, P. Zhang, E.W. McFarland, H. Metiu, CO_2 methanation on Ru-doped ceria, J. Catal. 278 (2011) 297-309.
[31] D.C. Upham, A.R. Derk, S. Sharma, H. Metiu, E.W. McFarland, CO_2 methanation by Ru-doped ceria: the role of the oxidation state of the surface, Catal. Sci. Technol. 5 (2015) 1783-1791.
[32] W. Gao, T. Zhou, Q. Wang, Controlled synthesis of MgO with diverse basic sites and its CO_2 capture mechanism under different adsorption conditions, Chem. Eng. J. 336 (2018) 710-720.
[33] D. Cornu, H. Guesmi, J.M. Krafft, H. Lauron-Pernot, Lewis acido-basic interactions between CO_2 and MgO surface: DFT and DRIFT approaches, J. Phys. Chem. C 116(11) (2012) 6645-6654.
[34] S. Jo, H.D. Son, T.Y. Kim, J.H. Woo, D.Y. Ryu, J.C. Kim, S.C. Lee, K.L. Gilliard-AbdulAziz, Ru/K_2CO_3–MgO catalytic sorbent for integrated CO_2 capture and methanation at low temperatures,

Chem. Eng. J. 469 (2023) 143772.
[35] F. Goodarzi, M. Kock, J. Mielby, S. Kegnæs, CO_2 methanation using metals nanoparticles supported on high surface area MgO, J. CO_2 Util. 69 (2023) 102396.
[36] H. Du, A nonlinear filtering algorithm for denoising HR(S)TEM micrographs, Ultramicroscopy 151 (2015) 62-67.
[37] S. Xie, Y. Liu, J. Deng, J. Yang, X. Zhao, Z. Han, K. Zhang, Y. Wang, H. Arandiyan, H. Dai, Mesoporous CoO-supported palladium nanocatalysts with high performance for o-xylene combustion, Catal. Sci. Technol. 8 (2018) 806-816.
[38] V.K. Lazarov, R. Plass, H.C. Poon, D.K. Saldin, M. Weinert, S.A. Chambers, M. Gajdardziska-Josifovska, Structure of the hydrogen-stabilized MgO(111)−(1×1) polar surface: Integrated experimental and theoretical studies, Phys. Rev. B 71(11) (2005) 115434.
[39] A. Kerrigan, K. Pande, D. Pingstone, S.A. Cavill, M. Gajdardziska-Josifovska, K.P. McKenna, M. Weinert, V.K. Lazarov, Nano-faceted stabilization of polar-oxide thin films: The case of MgO(111) and NiO(111) surfaces, Appl. Surf. Sci. 596 (2022) 153490.
[40] A. Misol, I. Giarnieri, F. Ospitali, A. Ballarini, J. Jiménez-Jiménez, E. Rodríguez-Castellón, F.M. Labajos, G. Fornasari, P. Benito, CO_2 hydrogenation over Ru hydrotalcite-derived catalysts, Catal. Today 425 (2024) 114362.
[41] S.J. Han, Y. Bang, H.J. Kwon, H.C. Lee, V. Hiremath, I.K. Song, J.G. Seo, Elevated temperature CO_2 capture on nano-structured MgO–Al_2O_3 aerogel: Effect of Mg/Al molar ratio, Chem. Eng. J. 242 (2014) 357-363.
[42] L. Li, X. Wen, X. Fu, F. Wang, N. Zhao, F. Xiao, W. Wei, Y. Sun, MgO/Al_2O_3 sorbent for CO_2 capture, Energy & Fuels 24 (2010) 5773-5780.
[43] J. Baltrusaitis, J. Schuttlefield, E. Zeitler, V.H. Grassian, Carbon dioxide adsorption on oxide nanoparticle surfaces, Chem. Eng. J. 170 (2011) 471-481.
[44] H. Du, C.T. Williams, A.D. Ebner, J.A. Ritter, In situ FTIR spectroscopic analysis of carbonate transformations during adsorption and desorption of CO_2 in K-promoted HTlc, Chem. Mater. 22 (2010) 3519-3526.